Plasmon - Interband Coupling in Nickel Nanoantennas

Zhaleh Pirzadeh[1], Tavakol Pakizeh[2], Vladimir Miljkovic[1], Christoph Langhammer[1] and Alexandre Dmitriev[1]*

[1] Department of Applied Physics, Chalmers University of Technology, 41296 Gothenburg, Sweden

[2] Faculty of Electrical and Computer Engineering, K. N. Toosi University of Technology, 16315 Tehran, Iran

[*]clangham@chalmers.se

KEYWORDS: Localized surface plasmon resonance, interband transition, nickel, nanoantenna, strong coupling.

ABSTRACT: Plasmonic excitations are usually attributed to the free electron response at visible frequencies in the classic plasmonic metals Au and Ag. However, the vast majority of metals exhibit spectrally localized interband transitions or broad interband transition backgrounds in the energy range of interest for nanoplasmonics. Nevertheless, the interaction of interband transitions with localized plasmons in optical nanoantennas has hitherto received relatively little attention - probably because interband transitions are regarded as highly unwanted due to their

strong damping effect on the localized plasmons. However, with an increasing number of metals (beyond Au and Ag) being considered for nanoplasmonic applications such as hydrogen sensing (Pd), UV-SERS (Al) or magnetoplasmonics (Ni, Fe, Co), a deeper conceptual understanding of the interactions between a localized plasmon mode and an interband transition is very important. Here, as a generic example, we examine the interaction of a localized (in energy space) interband transition with spectrally tunable localized plasmonic excitations, and unearth the underlying physics in a phenomenological approach for the case of Ni disk nanoantennas. We find that plasmon-interband interactions can be understood in the classical picture of two coupled harmonic oscillators, exhibiting the typical *energy anticrossing* fingerprint of a coupled system approaching the strong-coupling regime.

TEXT: The optical response of metal nanoparticles is distinctly different compared to their bulk counterparts due to the resonant collective oscillation of free electrons, so-called localized surface plasmon resonance (LSPR). The frequency of the LSPR oscillation can be controlled actively through the size and geometry of the particles as well as the surrounding medium, and can be well described by classical electrodynamics.[1] [2] [3] [4] Despite the dominant contribution of free electron LSPR to the optical properties of metal nanoparticle systems (in particular for the "classic" metals Au and Ag in the visible spectral range) for many other metals local (in energy space) or more global "backgrounds" of interband transitions (IBTs) also significantly affect their interaction with near-visible light. For example, in previous work, it has been shown that the LSPR response of Pd and Pt nanoparticles is strongly affected by the presence of a broad interband absorption background.[3] [5] [6] Other metals exhibit more spectrally localized IBTs – examples are Al (1.5eV), Cu (2.1eV), Fe (2.5eV) or Ni (4.7eV).[7] [8] Their interaction with LSPR has so far been investigated rather scarcely.[9] [10] [11] The latter is probably due to the fact that, in general terms in nanoplasmonics, bound electron transitions within or between bands are regarded as highly unwanted due to the attributed losses and damping of the LSPR. Hence, the interaction and coupling between localized plasmonic excitations of free electrons and IBTs has received little attention and is conceptually not well understood, let alone regarded as something potentially useful.

For this reason, in this work, we address in detail the interaction of a localized (in energy space) IBT with plasmonic excitations and unearth the underlying physics by analyzing experimentally and theoretically the case of Ni nanoantennas. We choose Ni as our model system because it has a spectrally localized IBT at ca. 4.7 eV in the UV, which conveniently allows us to spectrally tune and detune the LSPR from the IBT by means of nanofabricating

antennas with different size or by employing surrounding media with different refractive index to scrutinize the LSPR-IBT interactions. As the main result of that analysis we find that the LSPR – IBT interaction can be understood and described in a classical picture by two coupled harmonic oscillators. As we will show, the response of the LSPR-IBT system exhibits *energy anticrossing/frequency splitting*, which typically is observed in so-called strongly coupled systems and there referred to as Rabi splitting.[12] [13] [14] [15] [16]. Since the concepts that we develop and present in this work are generic, they are directly applicable to other metals featuring localized IBTs at near-visible frequencies.

We start by preparing arrays (covering cm^2 areas) of nickel nanodisks on fused silica substrates using hole-mask colloidal lithography.[17] This facilitates ensemble measurements of quasi-single particle optical properties. To probe the LSPR-IB interactions we steer the plasmon energy towards the bulk IBT energy of Ni in two complementary ways: (i) by tuning the Ni nanodisk diameter at constant height, and (ii) by varying the refractive index of the surrounding medium at constant Ni nanoantenna geometry. Figure 1a shows a series of optical extinction efficiency (i.e. optical cross-section normalized by projected Ni nanodisk area derived from SEM image analysis) measurements obtained for disks with different mean diameters (from 40 nm to 190 nm) at a constant height of 20 nm. Figure 1b shows corresponding analytical calculations based on the Modified Long Wavelength Approximation (MLWA)[18] [19] for oblate spheroids embedded in a homogeneous effective medium with refractive index 1.25, and by using a Ni dielectric function generated in the Drude-Lorentz framework by fitting the experimental data by Johnson-Christy[7] (see SI for details). As we have found earlier for other metals, the agreement between experiment and theory is more than reasonable in view of the simplifying assumptions in the model.[3]

From the measured and calculated data we make three main interesting observations. For decreasing disk size the LSPR is spectrally shifted towards the IBT resulting in (i) decreasing extinction efficiency of the low-energy (LE) peak (intuitively attributed to the LSPR), (ii) increasing extinction efficiency for the high-energy (HE) peak (intuitively attributed to the IBT), and (iii) a spectral shift of the latter towards higher energies as the LSPR "approaches". All these trends are nicely reproduced by the MLWA calculations.

In a second complementary experiment we again spectrally shift the LSPR with respect to the IBT in Ni but now without changing the nanodisk geometry/volume. This is achieved by evaporating a 20 nm thick SiO_2 film onto a sample with Ni nanodisks with 60 nm diameter and 40 nm height, to increase the average refractive index surrounding the disks from 1.25 to 1.5. Figure 1c features the corresponding extinction spectra before and after SiO_2 evaporation, respectively. As for the previous case we observe a change in the relative intensities of the two peaks, as well as a spectral shift of *both* peaks as the LSPR is pushed towards the IBT. Notably, this time we see this effect *without* altering the nanodisk geometry. The observed trends are again very well reproduced by our analytical MLWA calculations shown in figure 1d.

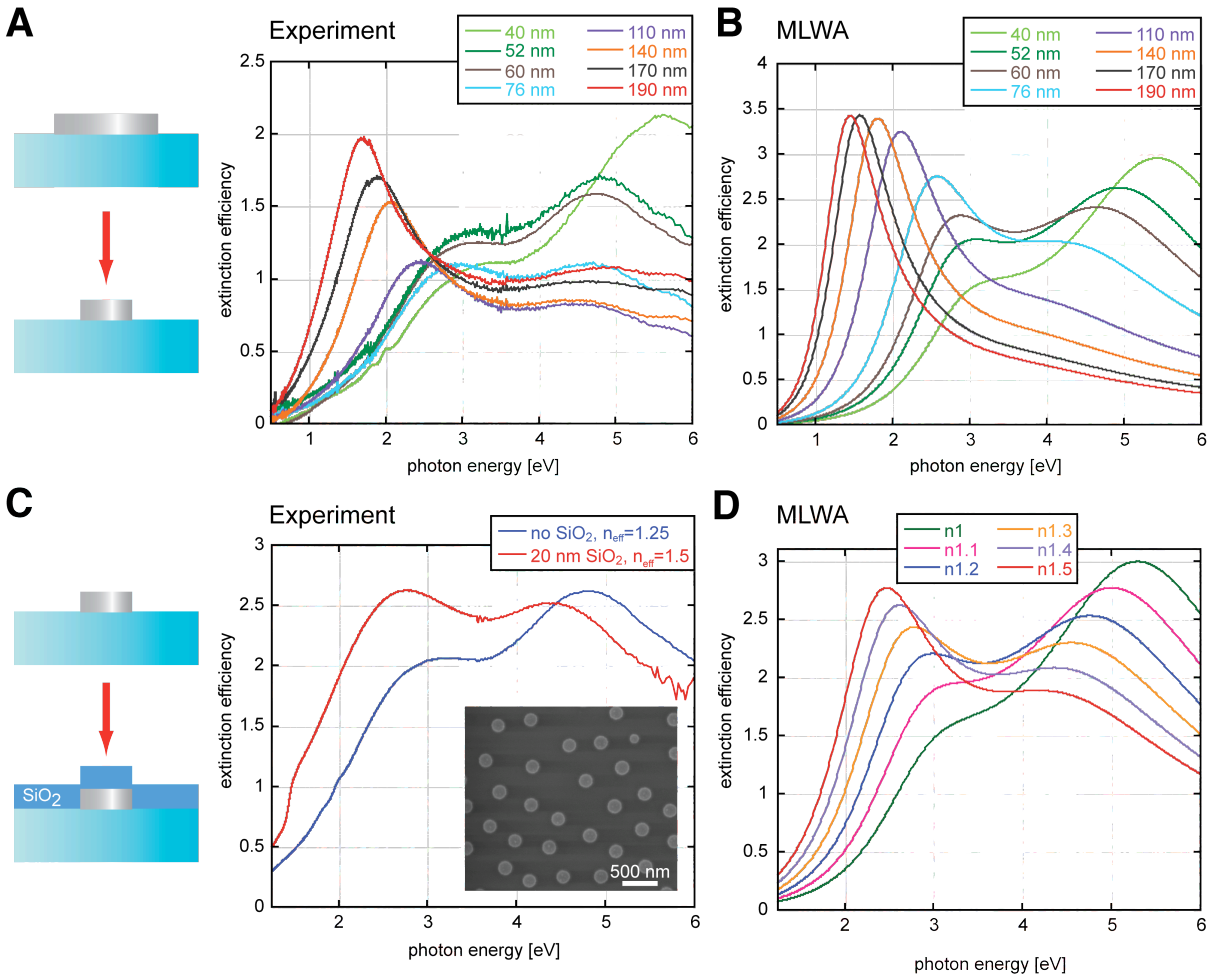

Figure 1. (a) Experimentally measured optical extinction efficiencies of arrays without long-range order (see inset in panel (c) for a SEM picture) of disk-shaped Ni nanoantennas with different diameters. We notice the emergence of a strong second peak at high energies when the low energy peak is spectrally shifted towards the interband transition at ca. 4.5 – 4.7 eV in Ni by decreasing the nanoantenna diameter. (b) Corresponding calculations for Ni oblate spheroids embedded in an effective medium carried out in the electrostatic modified long wavelength approximation (MLWA) framework reproduce nicely the key features observed in the experiment. (c) Alternative approach to spectrally shift the antenna LSPR resonance without changing its geometry by changing the refractive index of the surrounding medium. Experimentally this is realized by evaporating a 20 nm thick SiO2 film onto the sample, Ni disk

with D=60 nm and a thickness of 40 nm. Clearly, the relative intensities and spectral positions of the two observed peaks can be tuned in this way. (d) Corresponding MLWA calculations for a series of refractive indices show the trend observed in the experiment even more clearly.

The made observations are, at first sight, quite surprising, in particular the fact that the HE extinction peak - intuitively associated with the IBT in Ni - is spectrally shifted by several eV if the LSPR is pushed towards it. The former is rather improbable here because the IBT energy is determined by the bulk metal band structure only since the dimensions of the disks are far too large to exhibit quantum size effects. It is therefore useful to consider a simple mechanistic model of our system in terms of two harmonic oscillators: one representing the LSPR and the second one the IBT. This description is reasonable since, commonly, the dielectric functions of metals (and thus the fundamental band-structure-based properties determining IBTs and LSPRs) are well described by a Drude term and a/several Lorentzian oscillator term(s) accounting for the IBT(s). A system of two *coupled* harmonic oscillators *A* and *B* can be described analytically in a purely classical picture as pedagogically shown by Novotny[20], and have eigenfrequencies

$$\omega_{\pm}^2 = \frac{1}{2}\left[\omega_A^2 + \omega_B^2 \pm \sqrt{\left(\omega_A^2 - \omega_B^2\right)^2 + 4\Gamma^2\omega_A\omega_B}\right] \quad (1)$$

where

$$\omega_A = \sqrt{\left(k_A + \kappa\right)/m_A}\,, \quad (2)$$

$$\omega_B = \sqrt{\left(k_B + \kappa\right)/m_B} \quad (3)$$

and

$$\Gamma = \frac{\sqrt{\kappa/m_A}\sqrt{\kappa/m_B}}{\sqrt{\omega_A/\omega_B}} \quad (4)$$

with m_A and m_B being the mass of the two oscillators, k_A and k_B their spring constants and κ the coupling between the two. The solutions of eq. 1 are schematically illustrated in Figure 2 for two situations. First, we set $\kappa=0$ (i.e. the oscillators are uncoupled) and have $k_A=k_0$=const. and $k_B=k_0+\Delta k$, as well as $m_A= m_B=m_0$. As seen in Figure 2a, if we vary Δk from $-k_0$ to k_0 the eigenfrequency of oscillator B changes, whereas it remains constant for oscillator A. The two curves thus intersect at $\Delta k=0$. If we now introduce coupling, that is $\kappa\neq0$, the two curves don't intersect but instead exhibit *anticrossing* with a distinct frequency split, as seen in Figure 2b. Since the split is proportional to κ, the splitting increases with stronger coupling between the oscillators.[20]

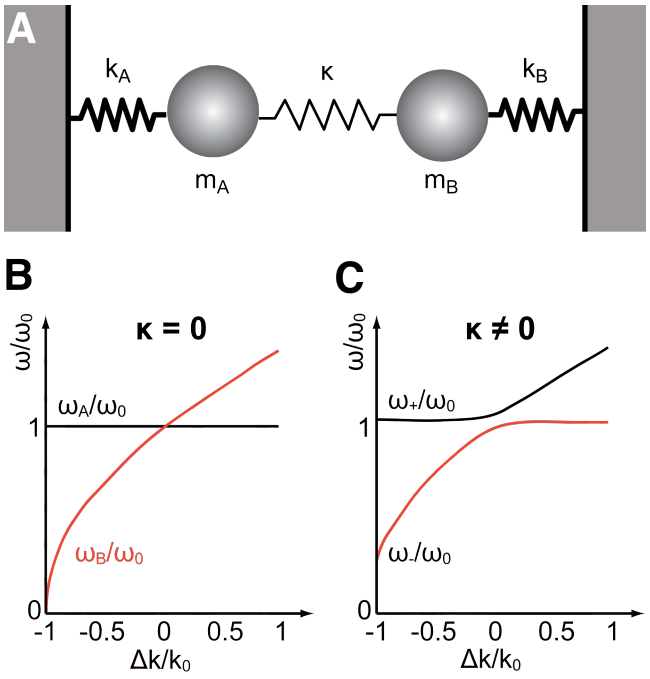

Figure 2. (a) Two coupled mechanical oscillators A and B with coupling κ, and spring constants k_A and k_B. (b) Schematic depiction of the eigenfrequencies of the two *uncoupled* ($\kappa=0$) oscillators with identical mass and spring constants $k_A=k_0$ and $k_B=k_0+\Delta k$ as a function of Δk. (c)

The eigenfrequencies of the coupled oscillators ($\kappa \neq 0$) exhibiting the characteristic frequency anticrossing as seen in strongly coupled systems.[20]

We now turn back to our Ni antennas to analyze our data in the above framework. As a first step of our analysis we plot, in Figure 3, the spectral positions of the LE and HE peaks observed in our experimentally measured, and in the MLWA extinction spectra as a function of the disk diameter (D). In addition, to highlight the (almost negligible) role of details in particle shape, we also plot the spectral positions of the LE and HE peaks as obtained from FDTD simulations of Ni disks (as opposed to oblate spheroids calculated by MLWA). In both cases the DL-dielectric function shown in the Methods section was used. For the LE-peak two scaling regimes can be identified. For large diameters the peak position is basically proportional to D and the system is in the material-independent regime, in line with what has been reported by Zoric et al. for other plasmonic metals.[3] For decreasing particle size, in the second scaling regime, a pronounced deviation from the D proportionality is observed and the LE peak energy asymptotically approaches a value around 3.5 eV both for the experiment and the simulated/calculated data. It is now interesting to look at the corresponding scaling of the HE-peak with D. We find, for large D, a basically constant value of ca. 4.5 eV in the experimental and FDTD data, and 4.1 eV for the MLWA calculations, respectively, which corresponds roughly to the Ni IBT energy (we conclude that the mismatch between experiment/FDTD and MLWA is related to the different shapes of particles – disks vs. oblate spheroids – calculated by the two methods). The HE peak starts to shift to higher energies for D < ca. 100 - 80 nm, i.e. when the LE peak starts to asymptotically approach the 3.5 eV limit by deviating from the D-proportionality. The most striking consequence is that a "forbidden zone" emerges, within which none of the two peaks is allowed. This behavior is thus the exact equivalent of the energy anticrossing behavior discussed

above for the coupled harmonic oscillators, where the LSPR constitutes the first and the IBT the second oscillator. In our experiment and calculations, varying the diameter of the Ni antenna (which shifts the LSPR frequency) has qualitatively the same consequence as varying the spring constant of oscillator *B* in the model. Thus, the IBT corresponds to oscillator A with *constant* k_A, as determined by the band structure of the metal.

To further highlight this analogy, in Figure 3 (black crosses), we also plot the peak position obtained in the MLWA framework when using a Drude dielectric function (i.e. no IBT term) with ω_P= 11.7 eV, γ_c=1.4 eV and ε_∞=3.6 eV. We find that for large D, the LE peak energy obtained in the experiment or by FDTD/MLWA using the DL dielectric function is in good agreement with the peak energy obtained when using only a Drude dielectric function. This is expected since in this regime, the dielectric response of Nickel is well described in the Drude framework. However, as the key result, when the LSPR energy calculated based on the Drude dielectric function approaches the regime where the anticrossing is observed in the experiment, the Drude LSPR peak energy shifts continuously across the forbidden zone. In other words, as expected in the absence of the IBT at 4.5 eV, no anticrossing is observed. This proves the importance of LSPR-IBT coupling for the energy split to occur. Interestingly, for further decreasing D, that is when posing the LSPR beyond the IBT, it is now the HE peak, which is proportional (but shifted in energy by roughly by the widths of the forbidden zone) the to the Drude LSPR. This is perfectly in line with the prediction made by Pakizeh[11], that is for small D it is the HE peak that carries the "signature" of the LSPR, whereas for large D it is the LE peak.

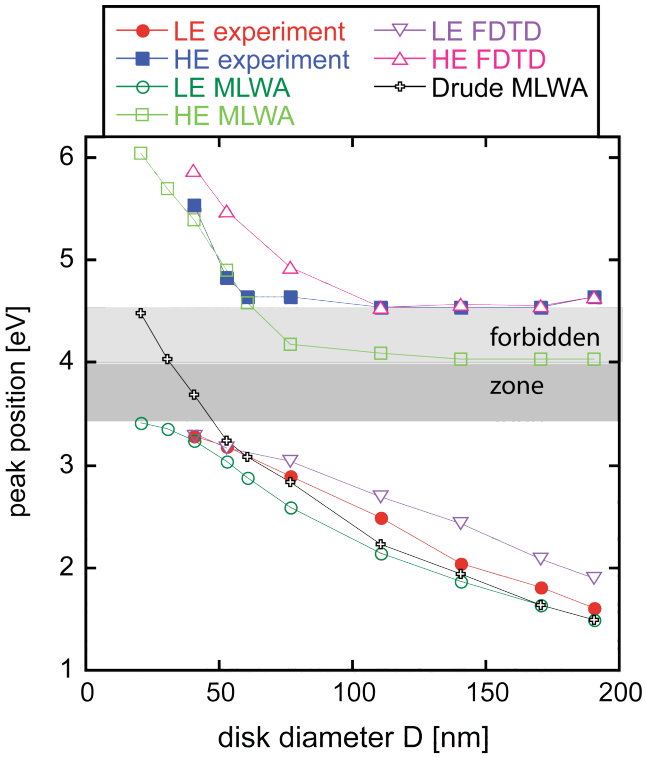

Figure 3. The spectral positions of the low-energy (LE) and high-energy (HE) peaks observed in the experiment and calculated by MLWA and FDTD plotted as a function disk diameter *D* for constant disk thickness of 20 nm. For decreasing particle size (D < 80 – 100 nm) a pronounced deviation from the initial D proportionality is observed and the LE peak energy asymptotically approaches a value around 3.5 eV. For the HE-peak, at large *D*, we find a constant value until, for *D* < 80 - 100 nm, the peak is shifted to higher energies. The most striking observation is a "forbidden zone" within which none of the two peaks is allowed. The latter is a direct manifestation of the energy anticrossing fingerprint for a coupled system in or approaching the strong coupling regime. The black symbols correspond to the LSPR energy calculated by MLWA using a Drude dielectric function, that is, without any interband contribution. For large *D*, the peak energy follows nicely the experimental and FDTD data. However, as the key result, when the LSPR energy calculated based on the Drude dielectric function approaches the regime where the anticrossing is observed in the experiment, the Drude LSPR peak energy shifts

continuously through the forbidden zone. In other words, as expected in the absence of the IBT at 4.5 eV, no anticrossing is observed.

A similar analysis for our second data set, that is nickel antennas with constant geometry tailored to achieve maximal coupling, where we vary the surrounding dielectric environment is shown in Figure 4. We plot the peak positions for the HE and LE peaks obtained from the experiment and the MLWA calculations as a function of the refractive index (RI) of the surrounding medium. As we, by changing the RI, spectrally shift the LSPR we fine-tune the coupling between the IBT and the LSPR and push the latter above the forbidden energy zone by energy anticrossing.

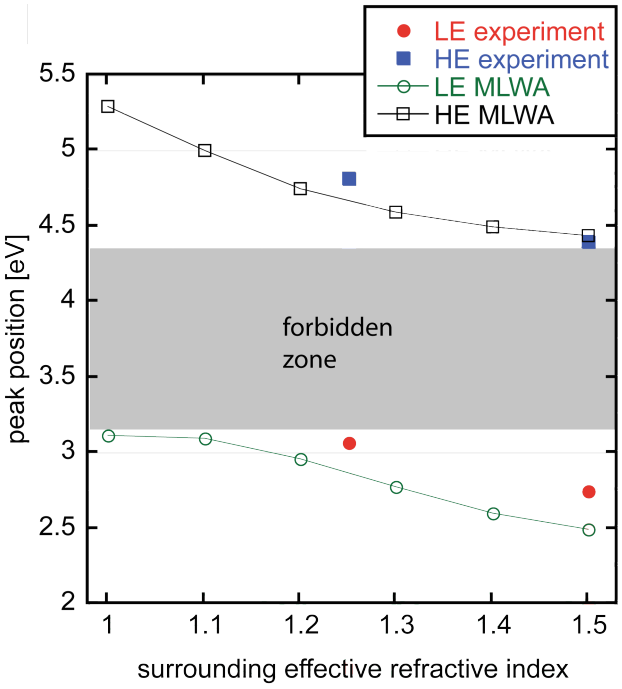

Figure 4: Peak positions for the HE and LE peaks obtained from experiment and MLWA calculations as a function of the refractive index (RI) of the surrounding medium for a constant

Ni antenna geometry in the LSPR-IBT coupling regime. By changing the RI to spectrally shift the LSPR we fine-tune the coupling between the IBT and the LSPR.

To further verify the strong mutual coupling of the LSP and IBT oscillators, it is useful to analyze the optical near fields for different situations. For that purpose we performed a series of Finite-Difference Time-Domain (FDTD) numerical simulations to track the electromagnetic field distribution in our system for HE and LE peaks occurring in disks with different diameters D. The same DL-dielectric function that we used for our MLWA calculations was also used here. In Figure 5a the corresponding far-field extinction spectra are shown. Clearly the same features observed in the MLWA and in our experiments are nicely reproduced. We now pick four different diameters D that correspond either to the uncoupled/material independent regime (D=192 nm, D=114 nm), or the coupled regime (D=76 nm, D=52 nm) to analyze the near-field distributions of the corresponding HE- and LE-peaks. Clearly, for the uncoupled case the LE (and thus solely LSPR) peak shows a dipolar signature with significant field enhancement whereas the HE peak (IBT) exhibits no field enhancement. In contrast, in the coupled regime at both the LE and HE peak energies a dipolar signature with significant field enhancement is imprinted on the respective near field distributions. The latter indeed confirms the (strong) coupling picture we have introduced above, that is that for small D the coupled IBT-LSPR system exhibits two split resonances on either side of a forbidden energy gap.

Finally, we note that we expect only the dipolar mode to be excited in the Ni disks since they are thin (20 nm) and illuminated at normal incidence. Moreover, the disks size in the coupling regime is such (< 80 nm) that we expect to be in the quasistatic regime. Therefore, the observed

increased penetration of the field into the particle for small disks in the coupling regime in Figure 5b is not caused by the excitation of higher modes but due to a slight alteration of field distribution due to the coupling to the IBT.

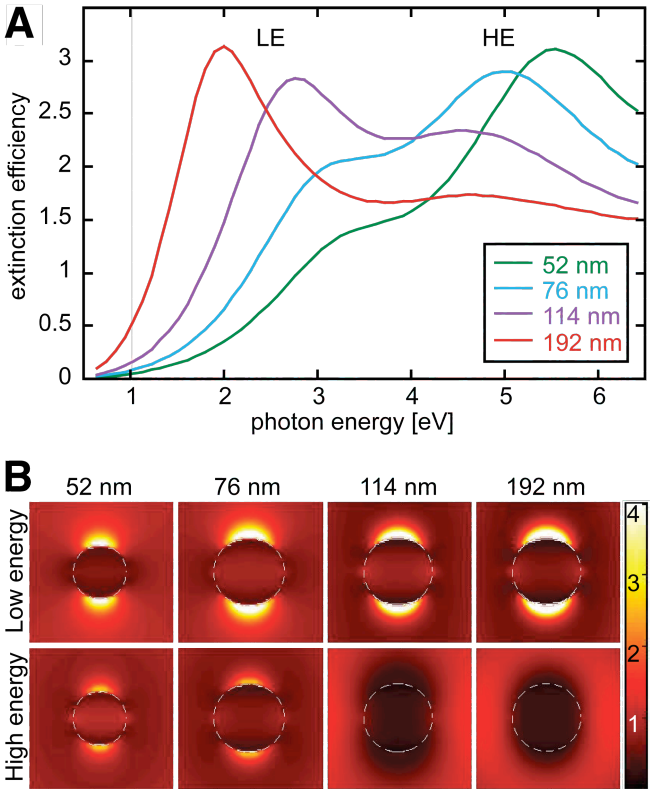

Figure 5. (a) Far-field extinction efficiency of nickel disks calculated by FDTD for a range of disk diameters for a constant height of 20 nm. (b) Corresponding near field enhancement plots at

the energies corresponding to the HE and LE peak for two antenna sizes in the uncoupled regime (114 nm, 192 nm) and in the coupled regime (76 nm, 52 nm). Clearly, in the uncoupled regime, the LE peak shows a dipolar signature with significant field enhancement and can thus be attributed to the LSPR, whereas the HE peak exhibits no field enhancement and can be attributed to the IBT. In contrast, in the coupled regime at both the LE and HE peak energies a dipolar signature with significant field enhancement is seen for the respective near field distributions.

In conclusion, we have demonstrated experimentally (by extinction measurements on Ni disk nanoantenna arrays without long-range order) and theoretically (by MLWA calculations and FDTD simulations) that LSPR-IBT interactions can be understood as two coupled harmonic oscillators that approach a strong coupling regime. The latter is manifested by an experimentally and theoretically observed energy anticrossing that occurs when pushing the LSPR towards and above the IBT by means of (i) tailoring the antenna diameter or (ii) its dielectric surrounding. We postulate that our phenomenological concept is generic and thus directly applicable to other metals exhibiting LSPR and spectrally localized IBTs, such as Al, Cu, Fe or Co. Moreover, we hope that it may stimulate further investigations to elucidate in detail the conceptual similarity with Rabi splitting in quantum systems and it's implications for nanoplasmonic systems that interact with interband transitions. Specific issues to be addressed are, for example, that the width of the energy split observed in the Ni system (ca. 1.1 eV) is proportional to the strength of the coupling and that the linewidths of the two resonances (for a 60 nm disk) are of the order of 1.4 eV (LE) and 3.6 eV (HE). In other words, the sum of the linewidths is significantly larger than the frequency split. This implies that damping has to be considered in a more quantitative analysis and that the present case can't be formally regarded as a "truly strongly coupled system".

Methods

Drude-Lorentz Model of the Nickel Dielectric Function

For our FDTD and MLWA simulations and calculations, respectively, we used the complex dielectric function of Nickel as calculated using the Drude-Lorentz Model according to:

$$\varepsilon(\omega) = \varepsilon_\infty - \frac{\omega_P^2}{\omega(\omega + i\gamma_c)} + \frac{G_0\omega_0^2}{\omega_0^2 - \omega^2 - i\Gamma\omega}. \qquad (5)$$

For the best fit to the experimentally determined dielectric function of Ni published by Johnson & Christy[7], we used the following parameters: ε_∞=3.6 eV; ω_P=11.7 eV; γ_c=1.4 eV; G_0=4.6; ω_0=4.9 eV; Γ=3.5 eV.

Corresponding Author

*E-mail: clangham@chalmers.se

Acknowledgements

We acknowledge financial support from the Swedish Research Council, the Swedish Foundation for Strategic Research (Framework Program "Functional Electromagnetic Metamaterials" RMA08 and "Functional Electromagnetic Metamaterials and Optical Sensing" RMA11-0037) and the Chalmers Area of Advance for Nanoscience and Nanotechnology, as well as valuable discussions with M. Käll, I. Zoric and T. Shegai.

References

1. Novotny, L.; Hecht, B.. *Principles of Nanooptics*. Cambridge University Press, 2006.
2. Kelly, K. L.; Coronado, E.; Zhao, L. L.; Schatz, G. C. The Optical Properties of Metal Nanoparticles: The Influence of Size, Shape, and Dielectric Environment. *J. Phys. Chem. B* **2008,** *107*, 668–677.
3. Zoric, I.; Zäch, M.; Kasemo, B.; Langhammer, C. Gold, Platinum, and Aluminum Nanodisk Plasmons: Material Independence, Subradiance, and Damping Mechanisms. *ACS Nano* **2011,** *5*, 2535–2546.
4. Bohren, C. F.; Huffman, D. R, *Absorption and Scattering of Light by Small Particles*. John Wiley & Sons: New York, 1998.
5. Hao, Q.; Juluri, B. K.; Zheng, Y. B.; Wang, B.; Chiang, I.-K.; Jensen, L.; Crespi, V.; Eklund, P. C.; Huang, T, J. Effects of Intrinsic Fano Interference on Surface Enhanced Raman Spectroscopy: Comparison between Platinum and Gold. *J. Phys. Chem. C* **2010,** *114*, 18059–18066.
6. Pakizeh, T.; Langhammer, C.; Zoric, I.; Apell, P.; Käll, M. Intrinsic Fano Interference of Localized Plasmons in Pd Nanoparticles. *Nano Lett.* **2009,** *9,* 882–886.
7. Johnson, P.; Christy, R. Optical Constants of Transition Metals: Ti, V, Cr, Mn, Fe, Co, Ni, and Pd. *Phys. Rev. B* **1974,** *9*, 5056-5070.
8. Palik, E. D., *Handbook of Optical Constants of Solids*. Academic Press: New York, 1991.
9. Wang, H.; Tam, F.; Grady, N. K.; Halas, N. J. Cu Nanoshells: Effects of Interband Transitions on the Nanoparticle Plasmon Resonance. *J. Phys. Chem. B* **2005,** *109*, 18218-18222.
10. Schwind, M.; Kasemo, B.; Zoric, I. Localized and Propagating Plasmons in metal Films with Nanoholes. *Nano Lett.* **2013,** *13*, 1743-1750.
11. Pakizeh, T. Optical Absorption of Plasmonic Nanoparticles in Presence of a Local Interband Transition. *J. Phys. Chem. C* **2011,** *115*, 21826-21831.
12. Bellessa, J.; Bonnard, C.; Plenet, J. C.; Mugnier, J. Strong Coupling between Surface Plasmons and Excitons in an Organic Semiconductor. *Phys. Rev. Lett.* **2004,** *93*, 036404.
13. Schwartz, T.; Hutchison, J. A.; Genet, C.; Ebbesen, T. W. Reversible Switching of Ultrastrong Light-Molecule Coupling. *Phys. Rev. Lett.* **2011,** *106*, 196405.
14. Ni, W.; Ambjörnsson, T.; Apell, S. P.; Chen, H.; Wang, J. Observing Plasmonic-Molecular Resonance Coupling on Single Gold Nanorods. *Nano Lett.* **2009,** *10*, 77-84.
15. Wiederrecht, G. P.; Wurtz, G. A.; Hranisavljevic, J. Coherent Coupling of Molecular Excitons to Electronic Polarizations of Noble Metal Nanoparticles. *Nano Lett.* **2004,** *4*, 2121-2125.
16. Yoshie, T.; Scherer, A.; Hendrickson, J.; Khitrova, G.; Gibbs, H. M.; Rupper, G.; Ell, C.; Shchekin, O. B.; Deppe, D. G. Vacuum Rabi Splitting with a Single Quantum Dot in a Photonic Crystal Nanocavity. *Nature* **2004,** *432* (7014), 200-203.
17. Fredriksson, H.; Alaverdyan, Y.; Dmitriev, A.; Langhammer, C.; Sutherland, D. S.; Zäch, M.; Kasemo, B. Hole–Mask Colloidal Lithography. *Adv. Mater.* **2007,** *19*, 4297-4302.
18. Wokaun, A.; Gordon, J. P.; Liao, P. F. Radiation Damping in Surface-Enhanced Raman Scattering. *Phys. Rev. Lett.* **1982,** *48*, 957-960.
19. Meier, M.; Wokaun, A. Enhanced Fields on Large Metal Particles: Dynamic Depolarization. *Opt. Lett.* **1983,** *8* (11), 581-583.

20. Novotny, L. Strong Coupling, Energy Splitting, And Level Crossings: A Classical Perspective. *Am. J. Phys.* **2010,** *78*, 1199-1202.

For Table of Contents Use Only

Plasmon - Interband Coupling in Nickel Nanoantennas

Zhaleh Pirzadeh[1], Tavakol Pakizeh[2], Vladimir Miljkovic[1], Christoph Langhammer[1] and Alexandre Dmitriev[1]*